Journal of Molecular Liquids 366 (2022) 120308

Contents lists available at ScienceDirect

Journal of Molecular Liquids

journal homepage: www.elsevier.com/locate/molliq

Dynamics of domain formation in a ferromagnetic fluid

Žiga Gregorin [a,b,*], Nerea Sebastián [a], Natan Osterman [a,b], Patricija Hribar Boštjančič [a,c], Darja Lisjak [a], Alenka Mertelj [a]

[a] Jožef Stefan Institute, Jamova cesta 39, 1000 Ljubljana, Slovenia
[b] Faculty of Mathematics and Physics, University of Ljubljana, Jadranska cesta 19, 1000 Ljubljana, Slovenia
[c] Jožef Stefan International Postgraduate School, Jamova cesta 39, 1000 Ljubljana, Slovenia

ARTICLE INFO

Article history:
Received 14 June 2022
Revised 30 August 2022
Accepted 5 September 2022
Available online 10 September 2022

Keywords:
Ferrofluids
Liquid magnets
Magnetic nanoplatelets
Domains
Domain growth dynamics
Differential dynamic microscopy

ABSTRACT

Ferrofluids are colloidal suspensions of magnetic nanoparticles. Ferromagnetic ordering – with spontaneous net magnetization in the absence of external fields – has been described for a system of permanently magnetic nanoplatelets suspended in *n*-butanol, concentrated enough to undergo the transition to the nematic phase. Such material shows magnetic domain structures analogous to those of solid-state ferromagnets. Through optimization of fundamental interactions, the threshold concentration for nematic ordering was reduced. The optimized material allows reproducible and controllable analysis of domain structures and their formation dynamics, with domains forming on the time scale of the order of seconds. Finally, the effect of an external applied magnetic field on the nematic director fundamental fluctuations inside a domain has been studied with differential dynamic microscopy. Interestingly, the results provide an estimation of the ferrofluid's spontaneous magnetization in the absence of external magnetic fields.

1. Introduction

Ferroic materials continue to be the subject of extensive research due to the growing demand for novel functional materials for technological advances [1–4]. Domains and domain structures are characteristic of ferroic materials and determine their behaviour and with it, their potential for applications, which rely mostly on their strong and specific response to external fields. In the case of ferromagnetic materials, magnetic domains account for regions in which the individual magnetic moments point in the same direction. Magnetic domains form to minimize the stray field energy and are divided by walls, in which magnetization changes direction [5]. Classical examples of ferromagnetic materials are iron, nickel and cobalt, which are all solid materials. In recent years a lot of development has also been done in soft matter materials that show interesting properties, such as the ability to manipulate rheological or other physical properties of a fluid with magnetic particles [6], experimental realisation of stationary topological solitons in a fluid chiral ferromagnet [7], reversible paramagnetic-to-ferromagnetic transformation of droplets with magnetic nanoparticles [8] and reconfigurable magnetic liquid crystal elastomers [9] are some of the examples.

Ferrofluids, i.e. colloidal suspensions of ferrimagnetic nanoparticles in an isotropic solvent, are despite their name paramagnetic. Thermal fluctuations impede magnetic interactions and the particles are dispersed with random orientations in the absence of external magnetic fields [10]. Common ferrofluids consist of spherical magnetic nanoparticles, and their stability and unique properties made them very interesting from the applicative point of view. Examples of usage for such materials have been demonstrated in magnetic dampers and seals or biomedical applications [11]. On the other hand, discotic nematic ordering can appear in suspensions of nanoplatelets above a threshold concentration that depends on the particle shape anisotropy and their electrostatic interaction [12–15]. In 2013 the first example of ferromagnetic liquid crystals was demonstrated when scandium-substituted barium hexaferrite (BHF) magnetic nanoplatelets were embedded in a liquid crystalline host [16]. Nanoplatelets have magnetic dipole moment perpendicular to the plane because of the high magnetocrystalline anisotropy of BHF. In this case, the combination of magnetic dipolar interactions and quadrupolar elastic nematic mediated interactions between the particles is such that the ferromagnetic ordering of the nanoplatelets is favourable inside the nematic matrix. Despite the low volume concentration of nanoplatelets (around 0.1 %), the combination of the nematic host proper-

* Corresponding author at: Jožef Stefan Institute, Jamova cesta 39, 1000 Ljubljana, Slovenia.
E-mail address: ziga.gregorin@ijs.si (Ž. Gregorin).

https://doi.org/10.1016/j.molliq.2022.120308
0167-7322/

ties and the nanoplatelets results in large magneto-optic responses (for much smaller magnetic fields than bulk nematic materials) and unique properties such as converse magnetoelectric effect [17]. A breakthrough came in 2016 when the first example of a true ferromagnetic ferrofluid was reported [18]. The authors demonstrated the formation of a colloidal nematic phase with spontaneous ferromagnetic ordering in a highly concentrated system of magnetic nanoplatelets suspended in an isotropic solvent. Such a system consisted of already mentioned BHF nanoparticles (thickness of 7 nm and average diameter of 48 ± 21 nm) functionalized with DBSA (dodecylbenzenesulfonic acid) surfactant and suspended in *n*-butanol. A threshold concentration of 28 vol% was reported for the appearance of the nematic ordering. Reported materials exhibited high sensitivity to small external magnetic fields (30 – 100 μT). By equilibrating the suspensions in the absence of external fields, Shuai et al. [18] demonstrated the formation of magnetic domains which is clear evidence of the ferromagnetic character of the suspensions. The large volume concentration needed for the formation of the ferromagnetic nematic phase, entailed long equilibration times, of the order of days, as reported in [18] for the development of clear domain structures.

It has been shown that the stability and formation of ferromagnetic ordering strongly depend on the electrostatic interactions between the particles, which can be tuned by the choice of solvent and the concentration of surfactant [19]. Additionally, magnetic interactions and particle-diameter distribution also crucially affect the threshold concentration [20]. Consequently, by varying the ferrofluid́s interparticle interactions the threshold concentration from isotropic to nematic phase was lowered for around 5-times to the one reported in the original publication [20]. More in-depth insight into this system came from small-angle neutron scattering (SANS) experiments, showing strong positional and orientational correlations of particles already in concentrated isotropic suspensions as well as in the ferromagnetic nematic phase [21]. Interestingly, results show that while correlations are only exhibited by the larger particles, the smaller ones contribute to a homogeneous background. Such results are in line with coarse-grained molecular dynamic computer simulations of mono- and polydisperse magnetic nanoplatelet systems, which highlight the importance of polydispersity in facilitating the transition into a nematic-like phase [22].

Newly obtained knowledge and the development of the material have made this research possible. Here, we demonstrate rapid domain formation, in the order of seconds, and we analyse formation dynamics. The stability of the domains to an external magnetic field is also studied. Additionally, we show the effect of different container thicknesses on the domain structure of ferromagnetic ferrofluid, mostly affecting wall thickness and not the shape of the domains. On the other hand, the longer slab of the material equilibrates in randomly sized and distributed domains. Finally, the demagnetization field is estimated from differential dynamic microscopy.

2. Material and methods

2.1. Preparation of suspensions

BHF nanoplatelets were synthesized hydrothermally [23] and suspended in 1-butanol using DBSA as a surfactant to ensure the stability of the suspension [24]. A detailed description of the synthesis protocol can be found in the Supporting Information. After the centrifugation procedure (Supplementary Note 1), the very diluted top part and the aggregates at the bottom are excluded from the material. The thickness of the nanoplatelets is calculated from SAXS measurements [19] and is mostly 3.3 nm (76 vol%) and 4.4 nm (22 vol%) with the remaining part (2 vol%) having larger thicknesses. The equivalent particle diameters are estimated from transmission electron microscopy (Jeol JEM-2100) images using DigitalMicrograph Gatan Inc. software to obtain a distribution with a mean diameter of 50 nm and a standard deviation of 18 nm. The saturation magnetization of the dried nanoplatelets was measured with a vibrating sample magnetometer (Lakeshore 7400 Series VSM) and is $M_p = 43$ Am^2/kg.

The threshold concentration for the transition from isotropic to nematic phase depends on the particle-diameter distribution, the magnetization of the nanoplatelets and the concentration of free surfactant in the suspension [20]. The concentration of the considered material after centrifugation is measured thermogravimetrically to the value of 5.3 vol% and the dry part of the suspension (particles and surfactant) has 12.3 wt% of surfactant. These values indicate that the material is above the transition point for the ferromagnetic nematic phase. In the present case, the drastic reduction of the threshold concentration in comparison to the material reported by [18] results in a lower viscosity. Additionally, a diluted sample with nanoplatelets concentration of 3 vol% was also prepared for calibration of our setup as discussed below.

For optical observation, the material is filled into borosilicate rectangular glass capillaries (VitroTubes Rectangle – Miniature Hollow Glass Tubing). Three different inner cross-sections are used: 20 μm × 200 μm, 30 μm × 300 μm and 40 μm × 400 μm. While the original length of the capillary is 50 mm they are cut to lengths around 20 mm before the sample is drawn in by capillary suction. The filled capillaries are then placed on standard 25 mm × 75 mm objective slides with the open ends sealed with a vacuum sealant (Agilent Torr Seal) to prevent evaporation of the solvent. A short slab of a few hundred micrometres is separated with a magnet from the bulk fluid for measurements, taking care on preserving the concentration.

2.2. Polarizing video microscopy and magnetic field compensation

As will be shown in the next section, the ferrofluids under study are remarkably sensitive to external magnetic fields, even as weak as the Earth's magnetic field. Thus, the material was studied with polarizing optical microscopy (POM) using a custom-built microscope with a red LED light source (wavelength 630 nm, FWHM 20 nm), Nikon 10x/0.30 Plan Fluor objective with a working distance of 16 mm and a monochrome camera (FLIR BFLY-U3-23S6M-C). The microscope's optical axis is in the vertical direction and the sample is placed on the holder horizontally. In this configuration gravity effects can be considered negligible for the employed capillary thicknesses (20, 30 and 40 μm). The sample holder is centred in an external field compensation system consisting of three orthogonal pairs of coils. Such a system allows us to compensate external magnetic fields down to 1 μT at the sample position (schematics can be found in Supplementary Fig. 1). Additionally, a static or dynamic magnetic field with an amplitude of up to 2 mT can be applied locally by an extra pair of coils aligned in the sample plane.

2.3. Cross-differential dynamic microscopy (c-DDM)

A detailed description of the Cross-Differential Dynamic Microscopy method can be found in the reference [25]. In the present case, experiments were performed in the POM setup described above, with an exposure time of 1 ms and a framerate of 460 FPS. "E10-O" geometry was used for recording, in which the polariser was rotated for 10 degrees and the analyser was perpendicular to the domain orientation. The image sequence was then Fourier

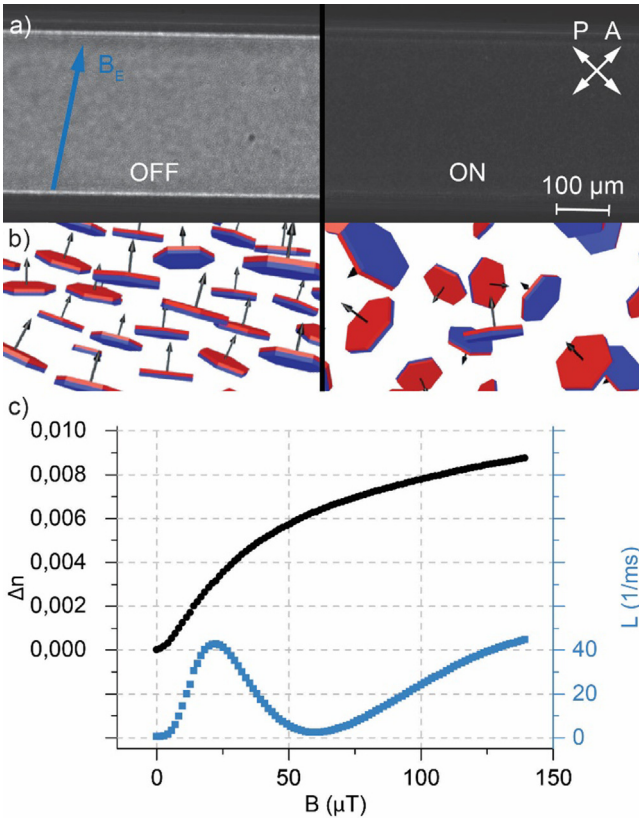

Fig. 1. The effect of external magnetic field on an isotropic fluid with $\phi = 3$ *vol*%. a) POM images show a material slab with external field-compensation turned off (left), which appears birefringent in Earth's magnetic field, and the same slab with the compensation turned on (right), showing the true isotropic character of the sample. The white arrows indicate the direction of polariser and analyser and the blue arrow is an estimation of external field direction (with the main contribution from Earth's magnetic field). b) Schematics of particle orientation. c) Calculated birefringence (black circles) and cross-polarised transmission (pixel intensity/exposure time in blue squares) as a function of magnetic field, applied along the capillary when the field compensation is enabled.

analysed as a function of time delay using an open-source package *cddm* to obtain the normalised image autocorrelation function with the *multitau* method [25].

In the case of concentrated suspensions with nematic ordering, c-DDM allows studying the orientational fluctuations of the director field in a similar way to traditional light scattering experiments. Assuming one elastic constant approximation, the relaxation times of fundamental modes as a function of the wave vector $\boldsymbol{q}$ and magnetic field $\boldsymbol{H}$ can be expressed as.

$$\frac{1}{\tau} = \frac{Kq^2 + \mu_0 \boldsymbol{H} \cdot \boldsymbol{M}}{\eta_{eff}} \quad (1)$$

where η_{eff} is the effective viscosity, K the orientational elastic constant of the liquid crystal [26] and $\boldsymbol{M}$ the sample magnetization.

3. Results

3.1. Field-induced birefringence in isotropic suspensions

Between crossed polarisers, the intensity of the transmitted light through a birefringent nematic material can be written as $I = I_0 \sin^2(2\theta) \sin^2(\pi d \Delta n/\lambda)$, where θ is the angle between the nematic director and the polarization of the incident light, d is the sample thickness, and Δn is the birefringence of the sample. Fig. 1 shows the effect of magnetic field compensation in the 3 vol% isotropic suspension. POM images show the transmitted intensity between crossed polarisers (at 45 degrees to the capillary axis) for the compensation system turned on and off. While the sample appears isotropic when the compensation is enabled, it appears birefringent when compensation is disabled. Such birefringence arises from the external magnetic field induced order and already for fields of the order of the Earth's magnetic field is $\Delta n \approx 0.006$ as shown in Fig. 1c together with the corresponding measured transmitted intensity. Δn for small fields rises quadratically and for larger fields starts to level out. Considering this, it is important to recall that all the observations reported in this work have been carried out with an enabled compensation system. Additionally, this points out that changes in transmitted intensity should be analysed carefully, as the application of field will result in both, changes of θ and Δn.

3.2. Ferromagnetic domains structures in short slabs

First, we focus on a short slab prepared in a 300 μm wide and 30 μm thick capillary. Initially, a strong, in-plane external magnetic field of 1.4 mT ($\boldsymbol{B}_{ann}$) is applied perpendicularly to the capillary axis. When removed, the sample is allowed to equilibrate for several seconds, after which a characteristic texture, with large birefringent domains, is obtained (Fig. 2). As shown by [18], these domains are uniformly macroscopic magnetized regions, in which magnetization $\boldsymbol{M}$ is directed along the nematic director $\boldsymbol{n}$. To minimize energy, uniformly magnetized materials tend to subdivide into magnetic domains. Each division results in a domain wall, in which magnetization rotates from one domain to another.

The fluidity of the sample, its relatively large saturation birefringence ($\Delta n \approx 0.03$) and the strong dependence of the latter on external magnetic fields, do not allow for investigating the magnetization direction of the domains via standard methods as the Kerr and Faraday's effect [27]. However, the fluidity of the sample enables easy manipulation of the ferromagnetic ordering via the application of a small magnetic field $\boldsymbol{B}_{bias}$ with a magnitude up to a few hundred μT. The application of such small fields contributes to the free energy by the magnetic term $U_M = -\boldsymbol{M} \cdot \boldsymbol{B}_{bias}$ which results in the displacement of the domain walls, expanding those favourable domains with magnetization in the same direction as the field and shrinking those with an unfavourable magnetization direction.

Central images in Fig. 2 show the final equilibrated domain structure after the removal of the annealing field ($\boldsymbol{B}_{ann} = 1.4$ mT) directed along the two possible in-plane directions perpendicular to the capillary axis (top row: $\boldsymbol{B}_{ann}$ was pointing to the left; bottom: $\boldsymbol{B}_{ann}$ was to the right). Both domain structures are complementary, with a slight shift of the central domain. The effect of small bias fields $\boldsymbol{B}_{bias}$ on the domain structure is shown in the left and right images of Fig. 2. When the annealing field $\boldsymbol{B}_{ann}$ is pointing to the left (top row), it can be seen that when $\boldsymbol{B}_{bias}$ is in the same direction as $\boldsymbol{B}_{ann}$, the central domain grows in size and the texture becomes more uniform. Simultaneously, the upper and lower domains get grainier, darker and smaller. When the $\boldsymbol{B}_{bias}$ direction is reversed, the opposite happens – the central domain shrinks and gets grainier while the upper and lower domains become brighter and grow in size.

The same configuration with crossed polarisers along and perpendicular to the capillary axis (Supplementary Fig. 2) shows that the lateral surface domains easily reorient if the bias field $\boldsymbol{B}_{bias}$ is applied in the same direction as $\boldsymbol{B}_{ann}$. The boundaries to the central domain, for which the reorientation allows a continuous deformation, fade. For the opposite $\boldsymbol{B}_{bias}$, such domains progressively shrink, due to the expansion of the domains at the menisci. The displacement of the domain wall, separating the central and the meniscus domain as a function of the applied $\boldsymbol{B}_{bias}$, is shown in Supplemen-

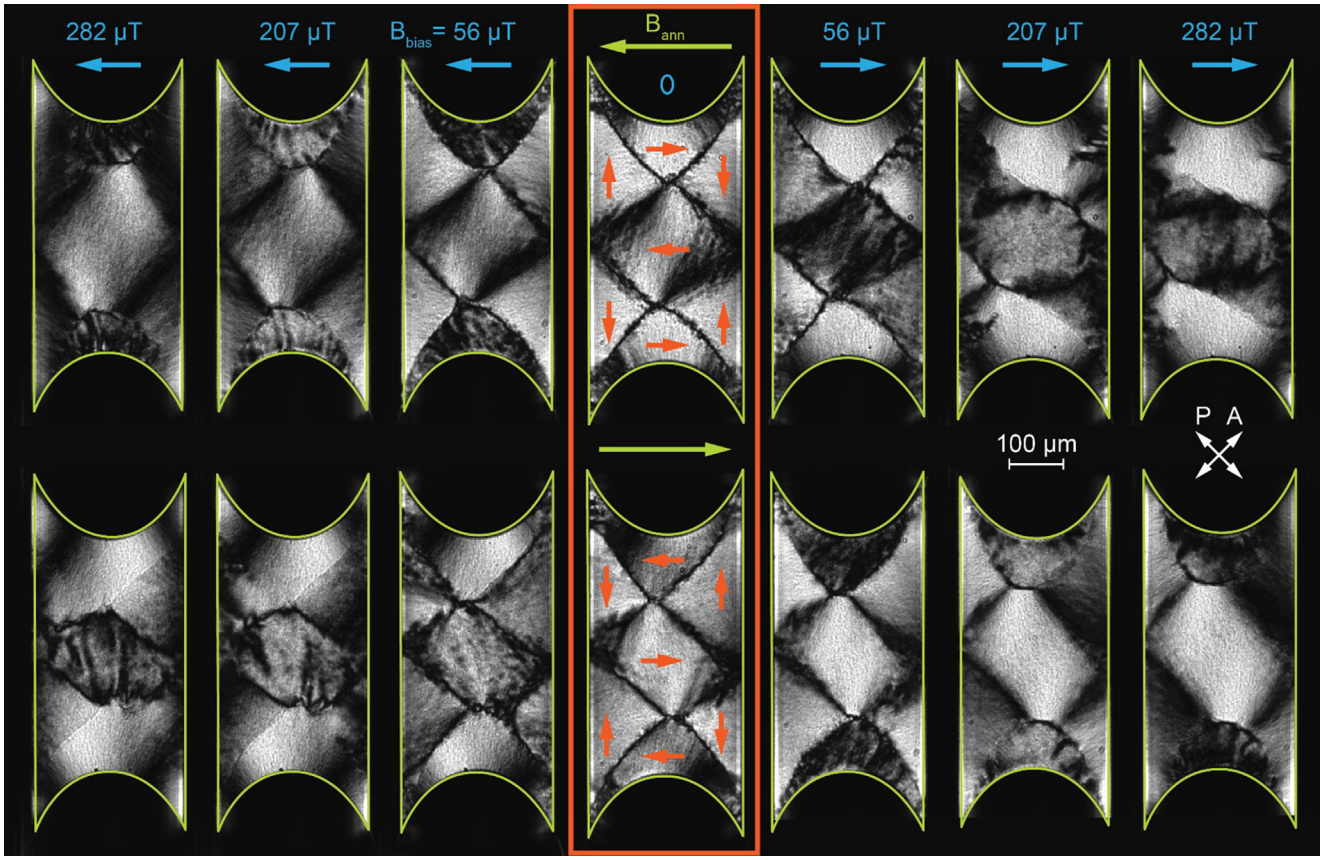

Fig. 2. Application of small bias magnetic field ($\boldsymbol{B}_{bias}$) with amplitudes of 56, 207 and 282 μT (direction marked with blue arrows) to the sample with domains annealed with the field $\boldsymbol{B}_{ann}$ in opposite directions (green arrow), i.e. to the left (top row) and to the right (bottom row). Direction of the domains after the annealing is marked with orange arrows. The sample is confined in a 300 μm × 30 μm glass capillary and placed between crossed polarisers (P-A) at 45 degrees.

tary Fig. 3. Thus, the observed changes under the application of a small field prove that in the studied geometry the central domain retains the same orientation as that induced by the initial annealing field $\boldsymbol{B}_{ann}$, whereas the upper and lower domains are oriented in the opposite direction. The magnetization of the four remaining side domains next to the capillary edges is directed perpendicularly to the annealing direction in such a way that the magnetization follows a closed flux path to minimize the total energy as marked in Fig. 2.

A comparison of top and bottom images in Fig. 2 reveals that the orientation of the magnetization loops in the final state can be controlled by the direction of the annealing field. In both cases, it is clear that $\boldsymbol{M}$ lies within the plane of the slab, as expected by the minimization of the magnetic charge on the surfaces. Accordingly, while in-plane fields of 10 μT are enough to manipulate the domains, out-of-plane fields of up to 1 mT are needed to observe any effect on the domain structure. To reorient the sample with out-of-plane fields, there is a competition between the contribution to the free energy coupling the magnetization and the field $f_{M,field} = -\mu_0(\boldsymbol{M} \cdot \boldsymbol{H})$ and the stray term, which for a 2D slab of material can be written as $f_{stray} = \mu_0 M_z^2/2$, where $\boldsymbol{M}$ is the sample magnetization and M_z its out-of-plane component. The stray energy will try to keep the magnetization in the plane of the slab preventing the reorientation. In the case of in-plane fields, however, there is no need to overcome this restriction.

In addition to domain growth/shrinkage, when applying small magnetic fields two effects can take place in the sample. On one side, in the same way as shown in Fig. 1 for the isotropic suspension the external magnetic field enhances the ordering of the nanoplatelets, increasing their birefringence (such effect will be discussed in the next section). On the other hand, due to the fluid character of the sample, the external magnetic field reorients the magnetization direction and thus the optical axis. Both affect the transmitted intensity of light, the latter being the stronger. Thus, while the transmitted intensity could be misleading in the interpretation of results due to its dependence on the applied field, the roughness of the texture is a fine indication of the sample order. As shown later (Fig. 3a, g) the application of large fields fully homogenizes the texture. When the material is left to equilibrate, the nematic order decreases and a grainy texture appears (central images in Fig. 2 and Fig. 3f, l). Such grains are evidence of a microstructure made of micro-domains, whose orientation slightly varies from one to the next. When small fields are applied parallel to the $\boldsymbol{M}$ of the domain, they slightly homogenize the texture, whereas when applied in the opposite direction, the grainy texture is enhanced.

3.3. Dynamics of the domain formation

Fig. 3 shows snapshots at different times of the domain formation for two orientations of the crossed polarisers. Snapshots correspond to Supplementary Video 1 and Supplementary Video 2. The sample is first exposed to $\boldsymbol{B}_{ann} = 1.4$ mT (Fig. 3a, g), which largely orients the nanoplatelets along the field direction (indicated by the green arrow in Fig. 3). However, while this is true in the centre of the slab, it can be seen that close to the boundaries magnetization starts to rotate in the direction parallel to the surface due to the minimization of the demagnetization field. Such an effect introduces a distortion on the uniform alignment that conditions

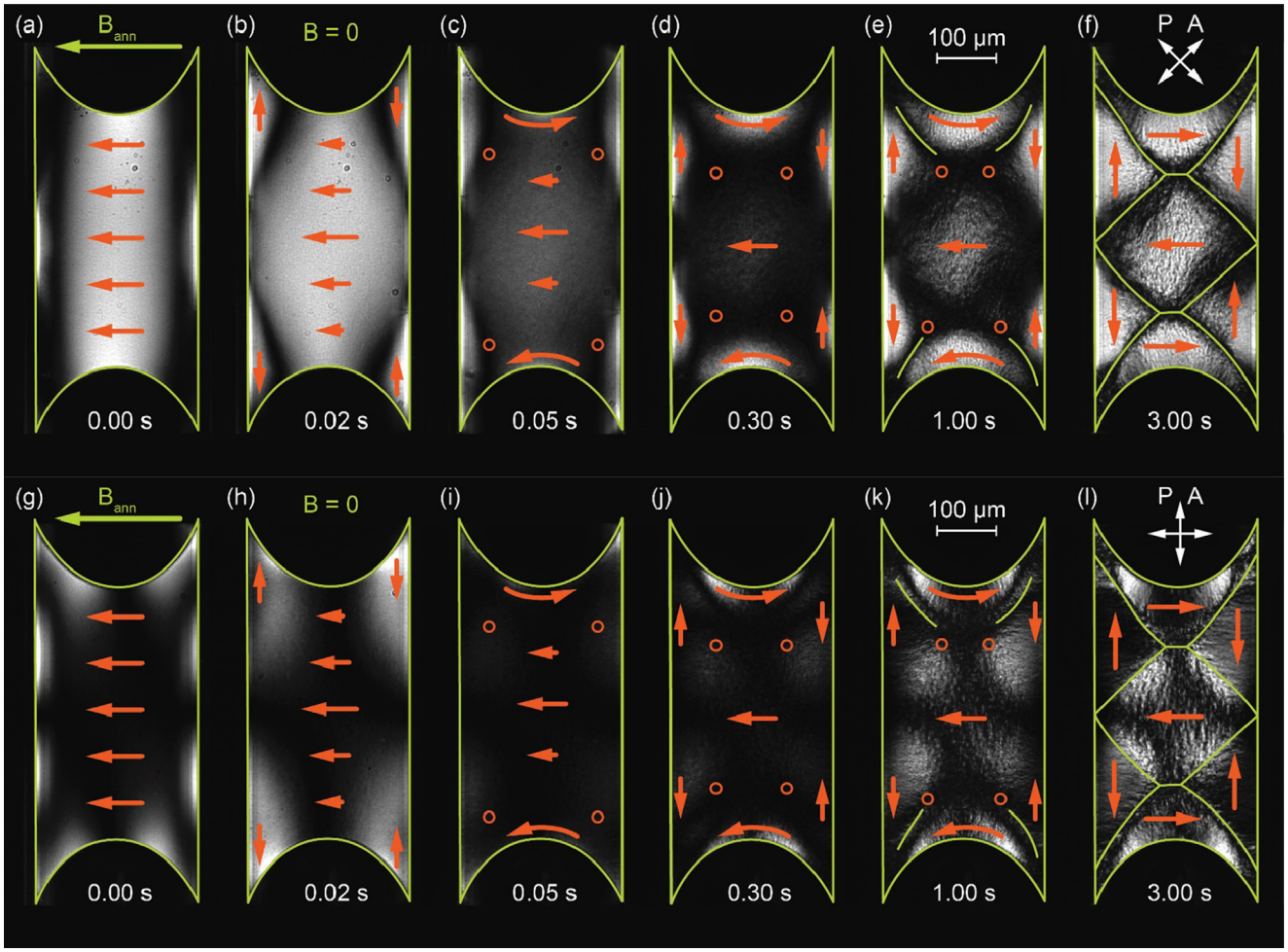

Fig. 3. Domain growth dynamics from annealing to the relaxed state. Top row corresponds to crossed polarisers oriented at 45 degrees with respect to the capillary axis, while bottom row is with crossed polarisers directed along the capillary axis (P-polariser, A-analyser). Orange arrows represent the evolution of the magnetization of the different areas. (a & g) Oriented sample with applied external magnetic field $\boldsymbol{B}_{ann} = 1.4\ mT$ marked with green arrow. (b & h) After field removal, sample starts reorienting at the corner areas, highly constrained by the boundary conditions. (c & i) The magnetization in top and bottom parts of the sample close to the menisci turn in the opposite direction. (d & j) Final orientation of the magnetization of the domains is established, with the boundaries between them being marked with circles. (e & k) The domain walls start to define from the menisci edges. (f & l) 3 s after field removal the sample has relaxed to the final state with fully grown domains.

the annealing process. Then, the annealing field is turned off (defined as time 0) and the nematic suspension is left in the zero-field environment. The strong constraints imposed by the surface boundaries trigger the fast reorientation of the material close to the menisci corners (Fig. 3b, h) with a characteristic time $\tau_g^{top} = 0.47$ s (more information in Supplementary Fig. 4), where the magnetization starts to reorient parallel to the edges of the capillary. Meanwhile, the large central part remains oriented in the annealing direction, although a slight increase of the characteristic microdomain roughness can be detected.

After 50 ms (Fig. 3c, i), transmitted intensity in the central part is significantly reduced (see Fig. 3c, with crossed polarisers at 45 degrees). The fact that transmitted intensity remains practically zero also for polarisers at 90 degrees, indicates that the director is not reorienting, but the birefringence is decreasing, i.e. the order of the sample is decreasing (from the saturated order induced when the annealing field is applied). While the central area continues its equilibration, the sample at the menisci saddles approaches the final state faster ($\tau_g^{top} < \tau_g^{central}$, plotted in Supplementary Fig. 4), as shown in Fig. 3d and j. As known from the final state shown in Fig. 2, at this stage menisci saddles should have already reverted the orientation of $\boldsymbol{M}$ to the direction of the annealing field. The faster response of these areas can be understood due to the effect of boundary surfaces. Simultaneously, the four side domains, also defined by the capillary boundaries, start to develop and grow towards the centre of the slab ($\tau_g^{side} = 1.33$ s). Such growth of domains starts to define those areas at which the magnetization switches direction from domain to domain, which will give rise to domain walls (Fig. 3e, k). The central domain continues to equilibrate to the final zero-field order. Equilibration time of the central domain ($\tau_g^{central} = 2.15$ s), already directed along the final orientation by the annealing field, is the longest, which might, initially, seem counterintuitive. However, it is important to note here that the central domain needs to accommodate the magnetic fields due to the developing surrounding domains. We shall return to this later in the discussion.

After 3 s in zero-field conditions, the relaxed state is obtained. Interestingly at this stage, considerable differences can be observed in the domain walls. While those boundaries separating the domains at the capillary edge and those in the menisci are more defined with an average thickness of the order of 10 µm, those boundaries of the central domain are not sharp and continuous reorientation of the magnetization span over larger distances, as clearly seen by the comparison of Fig. 3f and l. Over longer equilibration times of the order of 20 s, such boundaries progressively narrow to an average wall thickness of 13 ± 2 µm.

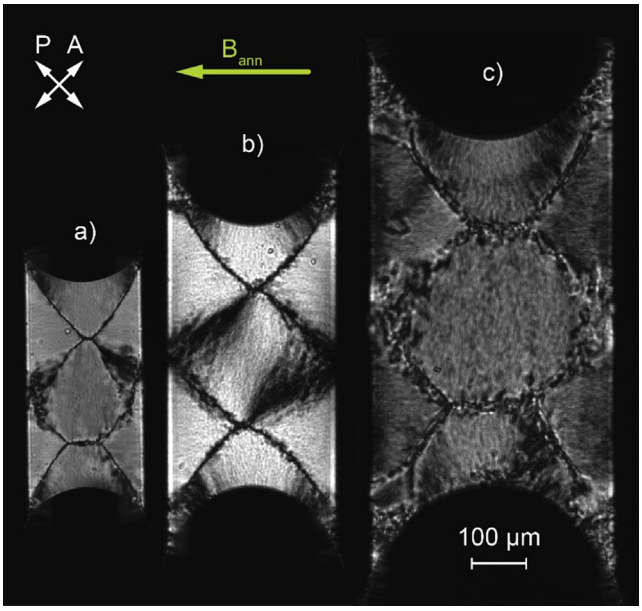

Fig. 4. Relaxed domain structure after annealing from 1.4 mT field in the direction of green arrow for different slabs of material with aspect ratio width/length around 0.6 and capillary thicknesses of 20, 30 and 40 µm from left to right.

3.4. Confinement and flow effects

Annealing fields parallel to the capillary long axis result in compatible structures (see Supplementary Fig. 5). The difference in the width-to-length ratio results in stretched domains along the material slab, divided by longer walls. For the standard annealing geometry, Fig. 4 shows the comparison of three domain structures obtained after relaxation for ferrofluid slabs with a different width but the same width-to-length aspect ratio (0.6) and with thicknesses of 20, 30 and 40 µm varying together with the width. Such an image nicely shows how domain size increases with the dimensions of the magnetic body. For a given capillary size, the increase in the length of the ferrofluids slab, and with it the aspect ratio, change the morphology of the domain structure, elongating those domains on the edge of the capillary (Supplementary Fig. 6). There is a limiting length above which the growth of domain size is energetically less favourable than division with new domain walls.

It is important to recall at this moment that the fluidity of the system has a great impact on the allowed domain morphologies, as there can exist numerous structures with the same energy. Thus, equilibration of the material slab over hours allows observing the development of more complicated domain structures, as shown in Fig. 5a. In this case, a slab with an aspect ratio of 0.6 was left to equilibrate overnight. Over this time, it slid along the capillary and additionally grew in size soaking up material from the main reservoir through the wet capillary surfaces. Both scenarios involve a flow of the material and resulted in a more complicated domain structure difficult to predict. One interesting observation is the equilibration of bend domain walls over time.

For very large ferrofluid slabs domain structure evolution is not predictable anymore. An example of a stable structure after a long time is shown in Fig. 5b. As in the case of the shorter slab, a strong tendency for bend structures can be observed. One should keep in mind that, in the present case, the reduction of the nanoparticles concentration, yet retaining nematic ordering, implies also the reduction of the spontaneous magnetization. Such lower magnetization makes deformations of the director energetically less expensive. Additionally, while splay deformation carries volume magnetic charge $\rho(\boldsymbol{r}) = -\nabla \cdot \boldsymbol{M}(\boldsymbol{r})$, twist and bend deformations are energetically more favourable, in agreement with those structures shown in Fig. 5b.

4. Discussion

The BHF ferrofluid presented here undergoes the transition to the nematic phase at a much lower concentration than examined

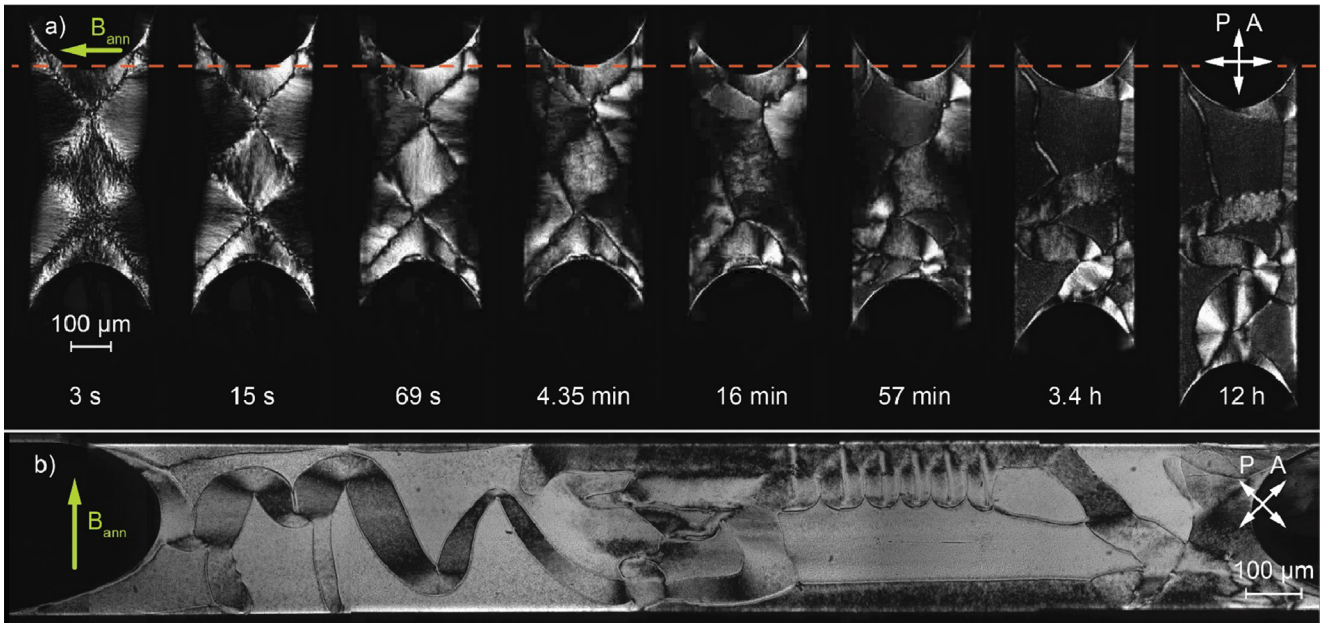

Fig. 5. Effect of flow in domain structures. (a) Stability of the domain structure in a short material slab over long time. The wet capillary edges favour the flow of material from the bulk reservoir (below, outside the field of view) enlarging the slab together with a small displacement. The sample was annealed from $\boldsymbol{B}_{ann} = 1.4$ mT (direction marked with green arrow). Orange dashed line serves as visual aid for the displacement. The slab after 12 h is 32 % larger and the flow resulted into formation of bend domains. (b) Equilibrated domain structure in a large material slab of 2 mm total length, 300 µm width and 30 µm thickness, after 20 h in zero-field. Structure was annealed from $\boldsymbol{B}_{ann}$ (marked with green arrow).

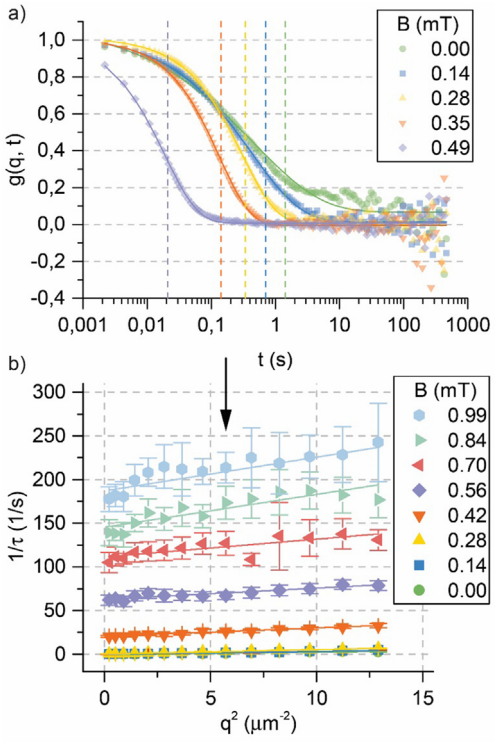

Fig. 6. DDM analysis. (a) Normalised correlation functions for some values of applied field $\boldsymbol{B}_{bias}$ at a given $q = 2.4\ \mu m^{-1}$ and the corresponding fits (lines). Dashed vertical lines correspond to the characteristic time τ. (b) Obtained relaxation rates $(1/\tau)$ as a function of q^2 for different fields. Solid lines give the linear fits. Black arrow marks the q^2 value corresponding to (a).

before [18]. The understanding and fine-tuning of inter-particle interactions allowed us to obtain ferromagnetic nematic ordering for concentrations as low as 5 vol%. The subsequently reduced viscosity resulted in fast and controlled annealing of magnetic domains as presented here.

The dynamics of the domain formation happen on the time scale of seconds and small magnetic fields with amplitudes of tens of μT. This allows us to probe the magnetic structures and determine the direction of magnetization of the domains. In short slabs, a well-known closed-loop domain pattern, such as those from the solid-state theory, forms with the handedness of the loop determined by the annealing field. Interestingly, despite retaining the orientation with the magnetization in the same direction as $\boldsymbol{B}_{ann}$, the central domain equilibration time is larger (1.2 s) than that of the domains in the menisci (0.34 s) or at the capillary surfaces (0.5 s), which are strongly affected by the boundary conditions. As demonstrated, this fluid magnetic system is exceptionally sensitive to small magnetic fields. During the domain formation, the central domain is not only relaxing from the saturated field-induced ordered state but is also adjusting to the field caused by the boundary domains.

To quantify such an effect, we measured by differential dynamic microscopy [25] the relaxation rates of the pure nematic fluctuation modes in a square area of 52 μm × 52 μm in the middle of the central domain under the application of an external magnetic field in the same direction as the magnetization of the domain. DDM enables access to lower and different wave vectors in a single measurement. For the measured E10-O geometry (see Section 2.3), the direction parallel to the applied field was analysed by fitting the autocorrelation functions obtained at different q values and fields to a stretched exponential function (Fig. 6a). The obtained relaxation rates $(1/\tau)$ show a quadratic dependence on q as expected from Eq. (1) (Fig. 6b). The quadratic coefficient and the constant term of such curves, yield the dependence on the applied magnetic field of K/η and $\mu_0 HM/\eta$ terms of Eq. (1) and are shown in Fig. 7.

For fields smaller than the critical $B_c = 342$ μT (extrapolated from the linear fit in Fig. 7b), the applied field does not have any effect on the relaxation rate of the nematic director fluctuation modes. For higher fields, the contribution of the magnetic term grows linearly. Effectively the second term in Eq. (1) can be then rewritten to.

$$\frac{\mu_0 \boldsymbol{M} \cdot (\boldsymbol{H} - \boldsymbol{H}_d(\boldsymbol{H}))}{\eta_{eff}}, \tag{2}$$

where $\boldsymbol{H}_d(\boldsymbol{H})$ accounts for the variation of the effective magnetic field arising from neighbouring domains. This demagnetization field will change with the reconfiguration of the domain structure driven by the applied external fields. In Fig. 7c and Supplementary Fig. 7, the measured area of interest is shown at different applied fields. It can be seen how the critical field in Fig. 7b-c (yellow-orange) corresponds to the field at which the central domain expands to the menisci. From this point onwards, the externally applied field cannot be compensated anymore by rearrangement of the domain structure, and the fluctuation rates drastically increase. It can be shown that the demagnetization field $\boldsymbol{H}_d(\boldsymbol{H})$ is proportional to the magnetization M_0, and the proportionality constant $\alpha(H)$ changes with the domain structure. At the critical field, we can assume the simplified case in which the magnetization of the slab is uniformly directed in-plane and perpendicularly to the capillary axis. The demagnetization field can be then calculated as $\boldsymbol{H}_d(\boldsymbol{r}) = -\nabla\phi_d(\boldsymbol{r})$, where the magnetic potential is given by.

$$\phi_d(\boldsymbol{r}) = \frac{1}{4\pi}\int \frac{\sigma_S(\boldsymbol{r}')}{|\boldsymbol{r} - \boldsymbol{r}'|} dS'. \tag{3}$$

Here $\sigma_S = M_0 \boldsymbol{m} \cdot \boldsymbol{z}$ is the surface magnetic charge distribution, being $\boldsymbol{m}$ a unit vector describing the direction of the magnetization and $\boldsymbol{z}$ is normal to the thin capillary edge surface. For the considered slab, with width 300 μm, length 500 μm and thickness 30 μm, a demagnetization field value of $H_d \sim 0.055 M_0$ is calculated in the centre of the slab, where DDM experiments were performed. Taking this result into account together with the critical field of 342 μT, $\mu_0 M_0$ can be estimated to be 6.3 mT, i.e. $M_0 = 5.0 \cdot 10^3$ A/m. One should bear in mind that this constitutes the limiting lower value for M_0, like the structure shown in Fig. 7c for the critical field should result in a lower proportionality constant due to the non-uniform orientation in the capillary boundaries. Nevertheless, such a value allows us to further estimate the polar order parameter P_1. For a completely oriented suspension, and considering the average particle size, magnetization and concentration of the sample, the saturated magnetization can be calculated as $M_{sat} = m_p \cdot \rho_p \cdot \phi = 1.15 \cdot 10^4$ A/m, where ρ_p is nanoplatelet density. With these values, $P_1 = M_0/M_{sat} = 0.44$.

For fields larger than B_c, several simultaneous effects complicate the interpretation of results. As we have seen in the case of the isotropic suspension, an applied field can increase the nematic order parameter S. Such change in the order parameter will further impact the values of viscosities and elastic constants as shown in Fig. 7a [28,29]. The intertwined magnetic field dependencies of all the parameters complicate the subsequent analysis of the DDM results. Additionally, it can be noted here that in the case of 0 μT and 70 μT, relaxation rates do not strictly follow Eq. (2), as two slightly different regimes, low-q ($q < 1.2\ \mu m^{-1}$) and high-q ($q > 1.2\ \mu m^{-1}$) can be discerned (see Supplementary Fig. 8). Such q-value corresponds to ~ 5 μm, in agreement with the above described grainy microstructure.

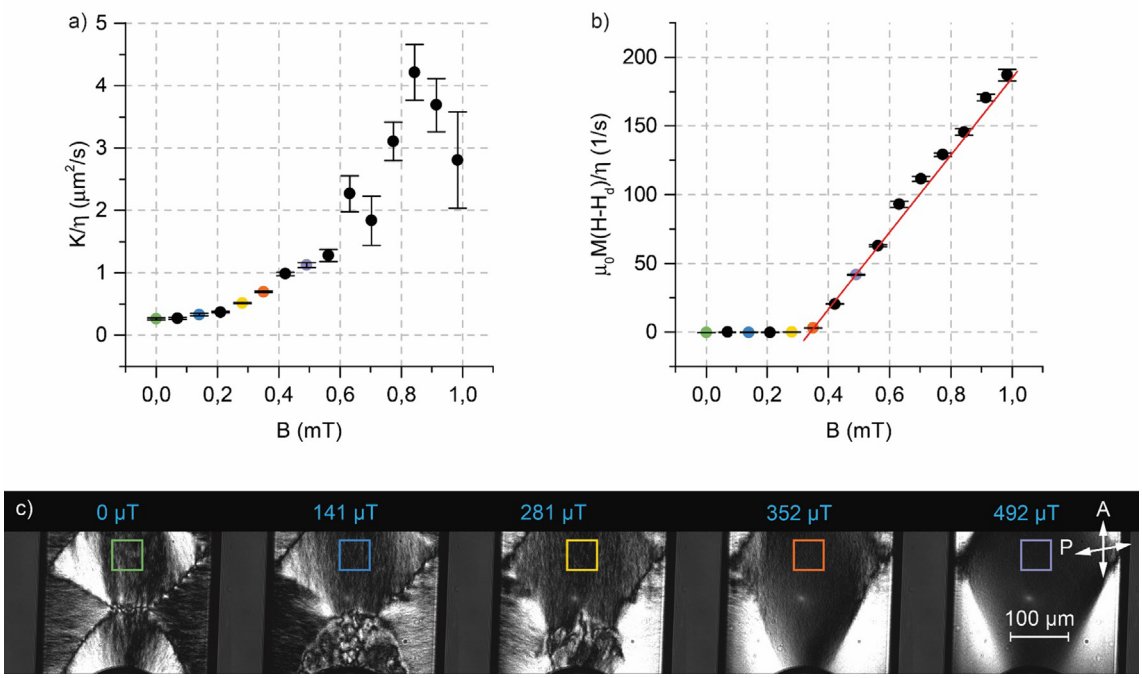

Fig. 7. DDM results for the square area with 52 μm side in the central domain in a material slab with aspect ratio $w/l = 0.6$. Polariser P is rotated for 10 degrees to the crossed direction. Slope a) and intercept b) terms of the linear fit to relaxation rates (Fig. 6b) in DDM in the parallel direction. c) POM images of the corresponding domain structure where DDM-analysed area is marked by the square. Square colours correspond to those of the coloured dots in a) and b).

One of the interesting differences we observed in the domain structures formed by these low-concentration ferromagnetic ferrofluids to those reported for the high-concentrated counterpart by Shuai [18] is the structure of the walls or regions dividing several domains. Shuai [18] reported a well-defined domain + 1 twist wall with a characteristic length of $\xi_M = \sqrt{K/\mu_0 M^2} < 1$ μm. Such characteristic length is the result of the balance between nematic elastic and magnetostatic energies. In the present case, however, different wall structures have been observed. Focusing on the central images in Fig. 2, it can be observed that the boundaries between those up/down oriented domains at the capillary edge and those shaped by the menisci are relatively sharp with no internal structure visible with the optical resolution. On the other hand, the boundaries defining the central domain span over large distances involving continuous and smooth changes in magnetization direction. This is in line with the reduced magnetization (6.5 mT) in comparison to the highly concentrated system described by Shuai [18] (40 mT), which makes deformations in the case of the presented ferrofluids energetically less expensive than in the previous case. As we have seen, this also results in a strong tendency to get bent domains and domain walls.

5. Conclusion

We studied the domain morphology and formation dynamics of low concentration nematic ferromagnetic suspensions of BHF nanoparticles in 1-butanol. Domains form on the time scale of the order of seconds and the handedness of the closed loop of the final domain structure can be tuned with the direction of the field used for annealing. The structure is easily probed with small magnetic fields of the order of tens of μT. The fluidity of the sample results in rather complex domain structures for large material slabs, where flow effects tend to promote bent domain structures and domain walls.

We have shown that while the domain structure accommodates to compensate external magnetic fields, the nematic director fundamental fluctuations remain unaltered at fields larger than the critical B_c.

CRediT authorship contribution statement

Žiga Gregorin: Investigation, Visualization, Methodology, Formal analysis, Writing – original draft. **Nerea Sebastián:** Investigation, Writing – review & editing. **Natan Osterman:** Supervision, Methodology, Writing – review & editing. **Patricija Hribar Boštjančič:** Resources. **Darja Lisjak:** Resources, Writing – review & editing. **Alenka Mertelj:** Conceptualization, Supervision, Formal analysis, Writing – review & editing.

Data availability

Data will be made available on request.

Declaration of Competing Interest

The authors declare that they have no known competing financial interests or personal relationships that could have appeared to influence the work reported in this paper.

Acknowledgement

This work was supported by the Slovenian Research Agency [grant numbers P1-0192, P2-0089, J1-2459, PR-08973, PR-08415]; Authors thank the Center of excellence in nanoscience and nanotechnology (CENN) Nanocenter for the use of TEM Jeol 2100 and Lakeshore 7404 vibrating-sample magnetometer.

Appendix A. Supplementary material

Supplementary data to this article can be found online at https://doi.org/10.1016/j.molliq.2022.120308.

References

[1] I. Dierking, S. Yoshida, T. Kelly, W. Pitcher, Liquid crystal–ferrofluid emulsions, Soft Matter 16 (2020) 6021–6031, https://doi.org/10.1039/D0SM00880J.
[2] M. Fiebig, T. Lottermoser, D. Meier, M. Trassin, The evolution of multiferroics, Nat. Rev. Mater. 1 (2016) 1–14, https://doi.org/10.1038/natrevmats.2016.46.
[3] T. Goršak, M. Drab, D. Križaj, M. Jeran, J. Genova, S. Kralj, D. Lisjak, V. Kralj-Iglič, A. Iglič, D. Makovec, Magneto-mechanical actuation of barium-hexaferrite nanoplatelets for the disruption of phospholipid membranes, J. Colloid Interface Sci. 579 (2020) 508–519, https://doi.org/10.1016/j.jcis.2020.06.079.
[4] N.A. Spaldin, R. Ramesh, Advances in magnetoelectric multiferroics, Nature Mater. 18 (2019) 203–212, https://doi.org/10.1038/s41563-018-0275-2.
[5] A. Hubert, R. Schäfer, Magnetic Domains: The Analysis of Magnetic Microstructures, Springer Science & Business Media, 2008.
[6] A.O. Ivanov, A. Zubarev, Chain Formation and Phase Separation in Ferrofluids: The Influence on Viscous Properties, Materials. 13 (2020) 3956, https://doi.org/10.3390/ma13183956.
[7] P.J. Ackerman, I.I. Smalyukh, Static three-dimensional topological solitons in fluid chiral ferromagnets and colloids, Nature Mater. 16 (2017) 426–432, https://doi.org/10.1038/nmat4826.
[8] X. Liu, N. Kent, A. Ceballos, R. Streubel, Y. Jiang, Y. Chai, P.Y. Kim, J. Forth, F. Hellman, S. Shi, D. Wang, B.A. Helms, P.D. Ashby, P. Fischer, T.P. Russell, Reconfigurable ferromagnetic liquid droplets, Science 365 (2019) 264–267, https://doi.org/10.1126/science.aaw8719.
[9] Y. Li, H. Yu, K. Yu, X. Guo, X. Wang, Reconfigurable Three-Dimensional Mesotructures of Spatially Programmed Liquid Crystal Elastomers and Their Ferromagnetic Composites, Adv. Funct. Mater. 31 (2021) 2100338, https://doi.org/10.1002/adfm.202100338.
[10] S. Odenbach, Colloidal Magnetic Fluids: Basics, Development and Application of Ferrofluids, Springer, 2009.
[11] S. Odenbach, Ferrofluids: Magnetically Controllable Fluids and Their Applications, Springer, 2008.
[12] J.-C.-P. Gabriel, P. Davidson, New Trends in Colloidal Liquid Crystals Based on Mineral Moieties, Adv. Mater. 12 (2000) 9–20, https://doi.org/10.1002/(SICI)1521-4095(200001)12:1<9::AID-ADMA9>3.0.CO;2-6.
[13] F.M. van der Kooij, K. Kassapidou, H.N.W. Lekkerkerker, Liquid crystal phase transitions in suspensions of polydisperse plate-like particles, Nature 406 (2000) 868–871, https://doi.org/10.1038/35022535.
[14] L. Onsager, The effects of shape on the interaction of colloidal particles, Ann. N. Y. Acad. Sci. 51 (1949) 627–659, https://doi.org/10.1111/j.1749-6632.1949.tb27296.x.
[15] D. van der Beek, P. Davidson, H.H. Wensink, G.J. Vroege, H.N.W. Lekkerkerker, Influence of a magnetic field on the nematic phase of hard colloidal platelets, Phys. Rev. E 77 (3) (2008) 031708, https://doi.org/10.1103/PhysRevE.77.031708.
[16] A. Mertelj, D. Lisjak, M. Drofenik, M. Čopič, Ferromagnetism in suspensions of magnetic platelets in liquid crystal, Nature 504 (2013) 237–241, https://doi.org/10.1038/nature12863.
[17] A. Mertelj, N. Osterman, D. Lisjak, M. Čopič, Magneto-optic and converse magnetoelectric effects in a ferromagnetic liquid crystal, Soft Matter 10 (2014) 9065–9072, https://doi.org/10.1039/C4SM01625D.
[18] M. Shuai, A. Klittnick, Y. Shen, G.P. Smith, M.R. Tuchband, C. Zhu, R.G. Petschek, A. Mertelj, D. Lisjak, M. Čopič, J.E. Maclennan, M.A. Glaser, N.A. Clark, Spontaneous liquid crystal and ferromagnetic ordering of colloidal magnetic nanoplates, Nat. Commun. 7 (2016) 10394, https://doi.org/10.1038/ncomms10394.
[19] P. Hribar Boštjančič, M. Tomšič, A. Jamnik, D. Lisjak, A. Mertelj, Electrostatic Interactions between Barium Hexaferrite Nanoplatelets in Alcohol Suspensions, J. Phys. Chem. C 123 (2019) 23272–23279, https://doi.org/10.1021/acs.jpcc.9b07455.
[20] P. Hribar Boštjančič, Ž. Gregorin, N. Sebastián, N. Osterman, D. Lisjak, A. Mertelj, Isotropic to nematic transition in alcohol ferrofluids of barium hexaferrite nanoplatelets, J. Mol. Liq. 348 (2022) 118038, https://doi.org/10.1016/j.molliq.2021.118038.
[21] A. Mertelj, B. Lampret, D. Lisjak, J. Klepp, J. Kohlbrecher, M. Čopič, Evolution of nematic and ferromagnetic ordering in suspensions of magnetic nanoplatelets, Soft Matter 15 (2019) 5412–5420, https://doi.org/10.1039/C9SM00949C.
[22] M. Rosenberg, Ž. Gregorin, P.H. Boštjančič, N. Sebastián, D. Lisjak, S.S. Kantorovich, A. Mertelj, P.A. Sánchez, The influence of polydispersity on the structural properties of the isotropic phase of magnetic nanoplatelets, J. Mol. Liq. 312 (2020), https://doi.org/10.1016/j.molliq.2020.113293 113293.
[23] D. Lisjak, M. Drofenik, Chemical Substitution—An Alternative Strategy for Controlling the Particle Size of Barium Ferrite, Cryst. Growth Des. 12 (2012) 5174–5179, https://doi.org/10.1021/cg301227r.
[24] S. Ovtar, D. Lisjak, M. Drofenik, Barium hexaferrite suspensions for electrophoretic deposition, J. Colloid Interface Sci. 337 (2009) 456–463, https://doi.org/10.1016/j.jcis.2009.05.041.
[25] M. Arko, A. Petelin, Cross-differential dynamic microscopy, Soft Matter 15 (2019) 2791–2797, https://doi.org/10.1039/C9SM00121B.
[26] P.G. de Gennes, J. Prost, R. Pelcovits, The Physics of Liquid Crystals, Phys. Today 48 (1995) 70–71, https://doi.org/10.1063/1.2808028.
[27] P.N. Argyres, Theory of the Faraday and Kerr Effects in Ferromagnetics, Phys. Rev. 97 (1955) 334–345, https://doi.org/10.1103/PhysRev.97.334.
[28] E. Jarkova, H. Pleiner, H.-W. Müller, H.R. Brand, Macroscopic dynamics of ferronematics, J. Chem. Phys. 118 (2003) 2422–2430, https://doi.org/10.1063/1.1533788.
[29] H. Pleiner, D. Svenšek, T. Potisk, H.R. Brand, Macroscopic two-fluid effects in magnetorheological fluids, Phys. Rev. E 101 (2020), https://doi.org/10.1103/PhysRevE.101.032601 032601.